https://doi.org/10.20965/jrm.2015.p0419

Paper:

A Wearable Haptic Device Based on Twisting Wire Actuators for Feedback of Tactile Pressure Information

M. Reza Motamedi, David Florant, and Vincent Duchaine

Control and Robotics Laboratory (CoRo), Department of Automated Manufacturing Engineering, École de Technologie Supérieure (ÉTS)
1100 Rue Notre-Dame Ouest, Montreal H3C 1K3, Canada
E-mail: {mohammadreza.motamedi.1@ens., vincent.duchaine@}etsmtl.ca

[Received December 20, 2014; accepted June 5, 2015]

This paper presents a novel wearable haptic device that provides the user with knowledge of a vertical force, measured at the fingertips, by applying pressure at three different locations on the user's body. Human prehension and manipulation abilities rely on the ability to convert tactile information into controlled actions, such as the regulation of gripping force. Current upper-limb prosthetics are able to partially replicate the mechanical functions of the human hand, but most do not provide any sensory information to the user. This greatly affects amputees, as they must rely solely on their vision to perform grasping actions. Our device uses a twisted wire actuator to convert rotational motion into linear displacement, which allows the device to remain compact and light-weight. In the past, the main shortcoming of this type of actuator was its limited linear range of motion; but with a slight modification of the principle, we have extended our actuator's linear range of motion by 40%. In this paper, we present the design of our haptic device, the kinematic and dynamic modelling of the actuator, and the results of the experiments that were used to validate the system's functionality.

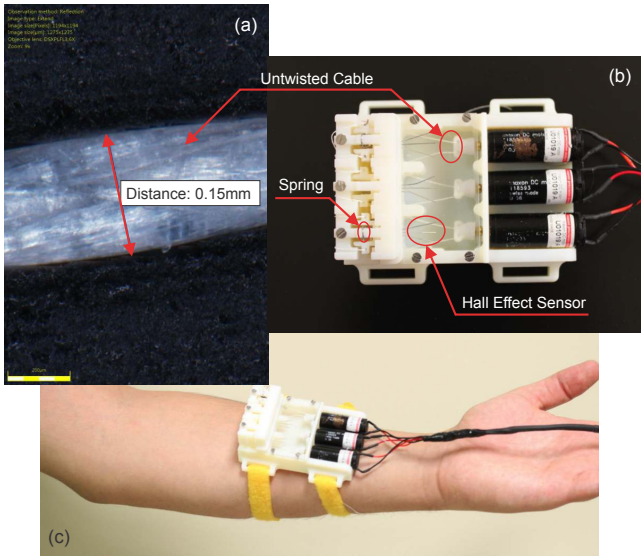

Fig. 1. (a) Microscopic view of a synthetic fiber spectra. (b) Top view of the haptic device using three Maxon DC motors, hall effect sensors and load springs. (c) Wearable haptic device placed on the glabrous skin of the human forearm.

Keywords: wire actuator, haptics, grasping force, touch sensitivity, static modality

1. Introduction

Recent years have seen haptic technology expand from research environments into daily life. Haptic feedback [1] is attracting greater attention in rehabilitation robotics, and an increasing number of studies are attempting to further the implementation of touch sensitivity in various applications [2–5]. However, due to the intrinsic locality of haptics and its involvement with a variety of environmental modalities, numerous challenges remain to be solved.

One area in which haptics seems most promising is the development of prosthetic limbs with sensory capabilities [6–8]. In current prosthetics, the need for an adequate safety margin requires amputees to pay continuous visual attention when accomplishing any task. Haptics can improve the lives of amputees because the stimulation of tactile receptors in healthy parts of their bodies can compensate for the absence of touch sensitivity in their prosthetics.

In order to function at the same level as the human sensory apparatus, amputees must be able to sense both static and dynamic events [9–11]. These tactile events in the human body are detected by an extensive network of tactile receptors [12, 13] that are spread throughout the skin area and that enable us to have the conscious perception of touch during skin contact. Sensation of these events can be restored using a haptic interface that applies normal stress [14], shear [15], or vibration [16] to the amputee's skin.

Our goal is to partially restore touch sensitivity to amputees. To this end, we aim to design a wearable haptic device [17] that restores the sensation of steady pressure (normal stress) under static conditions (**Fig. 1**). The preliminary studies conducted in our laboratory indicate that normal stress feedback alone, as opposed to vibrotactile or skin stretch stimuli, is sufficient for conveying tactile

pressure information. We hope normal stress feedback will allow amputees to recognize the level of force that is applied by the prosthesis as it interacts with the environment, such as when grasping an object. In our proposed mechanism, an orthogonal force is applied to the surface of the skin in order to activate the Merkel disk receptors [18] that respond to pressure on the skin.

This paper is organized as follows. Section 2 provides the context for our research, and discusses past developments in wire actuators. Section 3 then presents the kinematic and dynamic modelling of the actuator that was used in our device, followed by the overall mechanical design in Section 4. Our design is validated by our experiments, as shown in Section 5. The paper concludes with an evaluation of the system's performance, and a discussion of how it might be improved in further research.

2. Background

A previous user-oriented study, carried out in our laboratory, demonstrated that normal stress (vertical pressure), applied to healthy skin, is an optimal way to convey the sense of exteroceptive pressure to amputees. Building a device that can provide this type of feedback requires the use of a linear reciprocating actuator. Different types of actuators, including electro-active polymer actuators [19, 20], hydraulic or pneumatic actuators [21, 22], and magnetic actuators [23, 24] can be used. However, it is difficult to integrate most of these technologies into a lightweight and compact wearable haptic device, because even though the actuators themselves can be small, more components must be added on to the device in order to integrate the actuator with the sensor [25]. To circumvent this problem, we decided to use twisted wire actuators coupled with a compact direct drive conventional DC motor.

The principles behind the actuator's mechanism have, of course, been known for centuries. The wire actuator mechanism is based on the fact that when two wires are twisted together, their apparent lengths decrease. By fixing one end of the twisted wires to a motor shaft, and the other end to an object, it is possible to pull the object in a linear motion. More recently, a wire actuator was patented by Kremer in 1989 [26], and by Shoham in 2005 [27]. Wurtz et al. showed [28] that it is possible to mathematically predict the non-linear motion that is caused when the wires begin double-twisting. Double-twisting occurs when high rotational stress causes the fully twisted wires to re-twist around each other. However, although it is possible to predict the effects of double-twisting in theory, in reality it is almost always too complex.

In the field of robotics, twisted wire actuators first appeared in the literature in 1995 [29], when Kawamura et al. developed a high-speed mechanism for cable-driven robots by using wires to reduce the vibration of the system. In rehabilitation robotics, Godler and Sonoda presented a wire actuator for controlling an under-actuated robotic finger, followed by an entire robotic hand [30, 31].

Since twisted wire actuators feature elastic compliance, they are safe for direct contact with human skin even when they are operating at a very high transmission ratio. Furthermore, twisted wire actuators are ideal for use in haptic interfaces [32–35] because the twisted wires prevent backlash from occurring. This means that when the end effector reaches the maximum distance it can travel when applying pressure to the user's skin, the twisted wires prevent the effector from moving backwards, and no distance is lost as the effector simply stays put.

However, most of the twisted wire actuators used by past researchers are limited in terms of their wire length, and the resulting transmission ratios are low. In all the solutions that were presented in [30, 31, 36] the length of wire that can be twisted was specified by the distance between the movable parts of the mechanism and the motor shaft. As shown in [28], this allows a maximum displacement of just 46% of the untwisted wire length before double-twisting occurs. All of these results show that this type of mechanism, where the length of the wire is held constant, results in a low transmission ratio.

In order to improve the transmission ratio, we propose that the length of the wire should not be held constant; instead, the wires should be fed into the mechanism so that the length of the section of twisted wires can vary as necessary. This will result in both a higher transmission ratio and a more compact device. We present the kinematic and dynamic models of our modified twisted wire actuator in the following section.

3. Twisted Wire Actuator

3.1. Kinematic Analysis

The schematic view of the proposed mechanism is illustrated in **Fig. 2**. The two ends of a wire are attached to the motor shaft and passed through the holes separated by a constant distance, A, from the center of the shaft (**Fig. 2(a)**). As the two components, the shaft and the holes, are fixed at the same position (y-direction), when the mechanism is operating the distance d remains constant between the motor and the centers of the holes.

The distance d represents the fixed distance between the motor and the holes through which the wires pass. This distance is constant, as the positions of the motor and the holes remain fixed when the system is in action. L is the length of the wires between two points: the point at which they are attached to the motor, and the point at which they pass through the holes. Since the wires are twisting while the mechanism is in action, L is highly variable, as the twisting motion causes the wires to be pulled into the space of length d.

The planar projection of this process can be calculated using a triangle, shown in **Fig. 3(a)**, that represents the geometry of the untwisted wire. Here, the lengths of d and L remain constant, and L is a function of the angular position of the motor shaft. The third side of the triangle represents the horizontal projection of the wire, based on

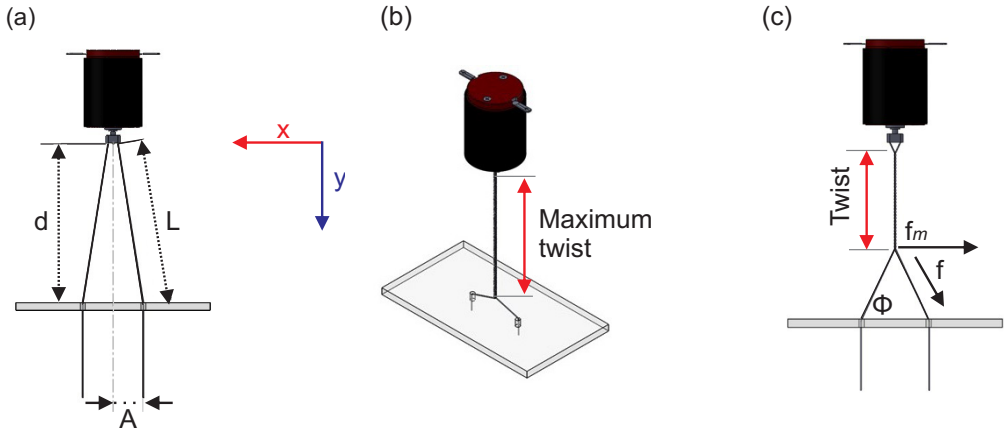

Fig. 2. (a) Original cable placement before twisting. (b) Maximum twisting of cable, before double-twisting occurs. (c) Diagram showing the system forces at the initial value and the final value.

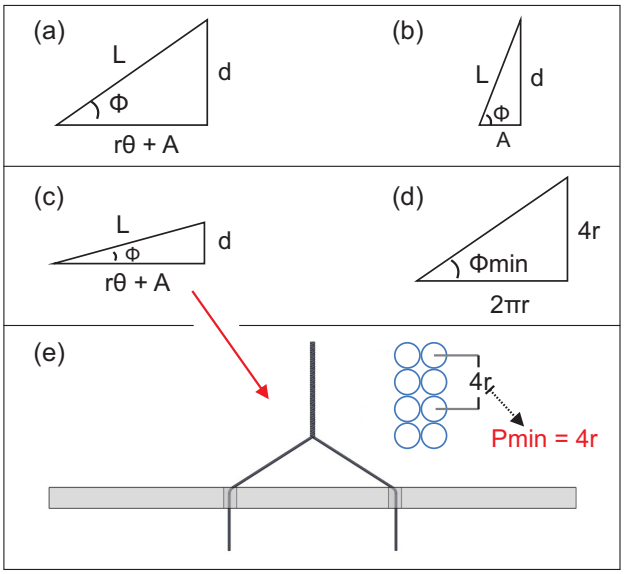

Fig. 3. (a) Initial arrangement of the mechanism. (b) Secondary arrangement of the mechanism. (c) Triangle representing the final values of the system's variables. (d) Triangle representing the final values of the system's variables with the $P_{\min}$. (e) View of the twisted wire in its final position.

its radius r, the angular position of the motor θ, and the distance between the two holes A.

$$L = \sqrt{(r\theta + A)^2 + d^2} \quad . \quad . \quad . \quad . \quad . \quad . \quad . \quad . \quad . \quad . \quad (1)$$

In the initial condition, i.e., when the wires are not twisted and the rotation angle is equal to zero (**Fig. 3(b)**), the wire length that corresponds to the hypotenuse of the triangle is called the initial length, L_0.

$$L_0 = \sqrt{A^2 + d^2} \quad . \quad . \quad . \quad . \quad . \quad . \quad . \quad . \quad . \quad . \quad . \quad (2)$$

Therefore, as the linear displacement given by the actuator is the result of the difference between the post-twisting length, L, and the pre-twisting length, L_0, this linear displacement can be represented as:

$$\Delta L = L - L_0 = \sqrt{(r\theta + A)^2 + d^2} - \sqrt{A^2 + d^2}. \quad (3)$$

As mentioned earlier, after a certain number of twists the wire begins to re-twist on itself by double-twisting. When double-twisting occurs, the relationship between the motor angle and the resulting linear displacement is difficult to predict using simple equations. Therefore, to avoid this unpredictability, we define the maximum possible displacement given by our mechanism as the maximum number of twists in the wire that can occur without inducing double-twisting.

To find the maximum possible displacement before double-twisting occurs, a series of equations must to be calculated. First, we define the maximum number of twists that can occur before double-twisting begins, as shown in **Figs. 3(c)** and **(e)**. This maximum occurs when the size of each node is equal to the sum of the diameter of the two wires.

$$P_{\min} = 4r \quad . \quad . \quad . \quad . \quad . \quad . \quad . \quad . \quad . \quad . \quad . \quad . \quad . \quad . \quad (4)$$

We are now able to define the minimum twisting angle, $\phi_{\min}$, and the maximum angular position of the motor, $\theta_{\max}$. With our knowledge that each twist gives $P_{\min} = 4r$, the minimum twisting angle is illustrated in **Fig. 3(d)**, and the maximum angular position of the motor is determined as:

$$\phi_{\min} = \tan^{-1}\frac{4r}{2\pi r} = \tan^{-1}\frac{2}{\pi} \approx 32.5^\circ \quad . \quad . \quad . \quad . \quad (5)$$

$$\tan\phi_{\min} = \frac{d}{r\theta_{\max} + A} \quad . \quad . \quad . \quad . \quad . \quad . \quad . \quad . \quad . \quad . \quad (6)$$

$$\theta_{\max} = \left(\frac{d}{\tan\phi_{\min}} - A\right) r^{-1} \quad . \quad . \quad . \quad . \quad . \quad . \quad . \quad (7)$$

Equation (7) describes the relationship between the angular motor displacement and the length of the twisted wires. Note that at this stage we have not yet taken into consideration the values of the static parameters. These will be included in the next section.

3.2. Static Analysis

Here we calculate the static equations in order to define the relation between the actuator torque and the load force that can be delivered from the mechanism. We also present the modelling of the physical aspects of the entire mechanism.

We know the net tension of the applied force to ends of the wires, which, as shown in **Fig. 2(c)**, allows us to verify the value of f_m. This value is a component of the force, f, and is perpendicular to the rotational access of the motor that creates the torque.

$$\sum F = 0 \quad \ldots \quad (8)$$

$$f_m = f\cos\phi \quad \ldots \quad (9)$$

By multiplying f_m by the given wire radius, the torque is equivalent to:

$$\tau_m = f_m r = fr\cos\phi. \quad \ldots \quad (10)$$

After replacing ϕ with the triangle elements shown in **Fig. 3(b)**, the geometries of the untwisted wire and the motor torque are as follows:

$$\cos\phi = \frac{r\theta + A}{L} \quad \ldots \quad (11)$$

$$\tau_m = fr\frac{r\theta + A}{\sqrt{(r\theta + A)^2 + d^2}}. \quad \ldots \quad (12)$$

Furthermore, as brand-name motors come with a pamphlet that gives the maximum torque (among other details), it is also useful to estimate the net load according to the rotation angle of the motor. Eq. (13) gives the relationship between the motor torque and force, and Eq. (14) gives the maximum force that can be applied by the mechanism.

$$R_m = \frac{r(r\theta + A)}{\sqrt{(r\theta + A)^2 + d^2}} \quad \ldots \quad (13)$$

$$f = \frac{\tau_m\sqrt{(r\theta + A)^2 + d^2}}{r(r\theta + A)} \quad \ldots \quad (14)$$

3.3. Validation Analysis

After developing the kinematic and static models of the twisted wire actuator, we must conduct an experiment to validate that the calculated formulas do indeed describe the exact behaviour of the proposed mechanism. To this end, we used a bench test to measure the linear motion and the linear force that was generated by the actuator through the wire transmission. The schematic view of the motor, and the housing that was initially used in this experiment, are shown in **Fig. 4**.

For the kinematic analysis, the relevant displacement of the prototype was determined as follows:

- The shaft was manually rotated. After every 5 rad, the linear displacement was measured using a micrometer. Unlike in the theoretical calculations, according to which the number of turns stopped at the end of the procedure, here the data acquisition was performed up to 45 rad due to the difficulty of manually exceeding this value for our prototype. In fact, because of the instability of this condition, it is difficult to obtain an accurate measurement of the displacement, especially after further turns.

- Turning up to 45 rad provided an adequate number of data for the comparison of the theoretical values. The data represent the range in which the torque produces a significant usable force to the end effector. **Fig. 4** shows the relationship between the linear and the angular displacements, as determined by the theoretical analysis (solid line) and by the results of the experiment (dashed line). The highlighted area indicates that the trends of the two curves are nearly identical. From this result, we conclude that our kinematic model can be used for designing the final prototype.

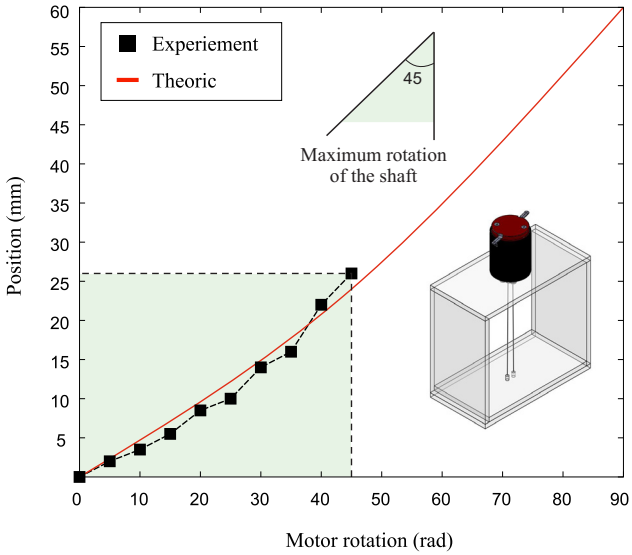

Fig. 4. Comparison between two analyses, each of which represent the kinematic system as based on the position angle of the motor. The dashed line is the experimental analysis, and the solid line is the theoretical analysis. These analyses were obtained using a bench test performed on the prototype shown in the bottom-right corner.

For the static analysis experiment, we attached a test weight to the end of the moving part and measured the displacement. By imposing a linear force on the mechanism, and by measuring the maximum torque as well as the maximum displacement, we were able to solve Eq. (14). The predictions we made using this formula are indicated by the dotted line without marks in **Fig. 5**. However, our predictions clearly do not match the results of the experiment.

We believe this discrepancy was caused by the torsional stiffness of the wire. Our equation assumes 100% mechanical efficiency, which is not a realistic depiction of actual task-oriented conditions, as it does not take variables such as stiffness into account. When the wires are twisted, each wire exerts some force on the other wire.

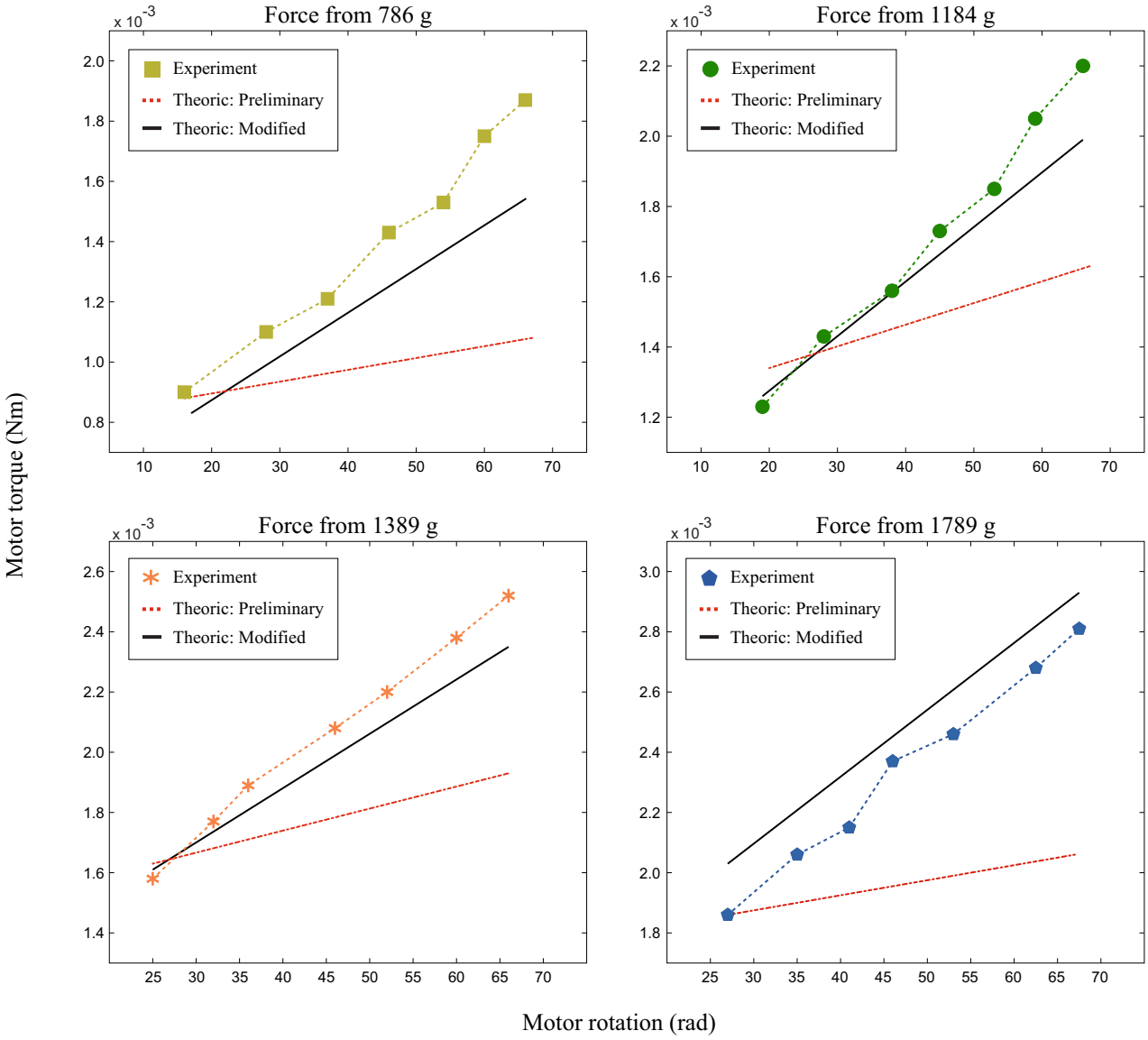

Fig. 5. Static analysis for comparisons between the preliminary theoretical data, the results of the experiments, and the modified theoretical data. During the experiments, four separate tests were conducted using laboratory test weights of 786 g, 1184 g, 1389 g and 1789 g. Note that the modified theoretical data have been modified by taking the torsional stiffness ($k = 1.65$) into consideration.

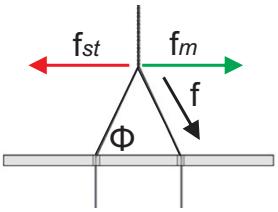

Fig. 6. Major forces applied to the mechanism.

These forces act in the opposite direction to the rotational angle of the twisted wire. This rotational stiffness can be expressed as:

$$\tau_s = k\Delta\theta. \quad \ldots\ldots\ldots\ldots\ldots\ldots (15)$$

As shown in **Fig. 6**, by considering the stiffness of the wire, (f_{st}), we can obtain the corrected force, f, and the corrected torque, τ_c,

$$(f_m - f_{st}) - f\cos\phi = 0 \quad \ldots\ldots\ldots\ldots (16)$$

$$\tau_c = f.r\cos\phi + k\theta. \quad \ldots\ldots\ldots\ldots (17)$$

We used trial and error to determine the stiffness factor, $k = 1.65$. The modified version of the static analysis, which is far more accurate, is illustrated by the solid lines in **Fig. 5**.

4. Mechanical Design

The core aim of the mechanical design is to create a device that can provide an orthogonal force by converting the rotary motion of the motor shaft into the linear move-

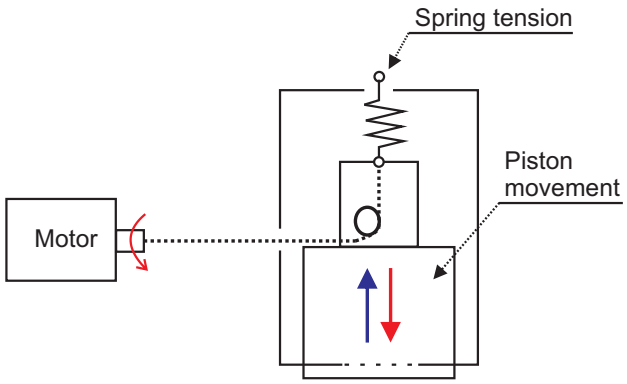

Fig. 7. Load spring used to move the piston.

ment of the piston. The pressure should then released using a spring. More specifically, an opposing spring force is continuously applied to the piston, which has the effect of moving the piston in the opposite direction. This results in the release of the twisted wires when the motor stops rotating. A miniature spring is placed on top of the piston, as shown in **Fig. 7**, in order to generate the force that is needed to return the piston to its initial position.

Note that the piston must be able to apply up to 10 N of force to the user in order to convey a variety of static modalities. In our mechanism, this requires a piston traveling distance of approximately 10 mm.

4.1. Main Body of the Device

In order to create a wearable haptic device, our device should be able to apply static pressure ranging from 1 to 10 N, while being compact and lightweight. Furthermore, the device should not become unresponsive or uncomfortable for the user during long periods of operation.

We used CATIA V5 for drawing, modeling, and assembling the haptic device (**Fig. 8**). We began prototyping after finding the critical parameters, such as the dimensions, lengths, edge curves, and the whole body structure. We used a rapid prototyping machine, Objet 24 from Stratasys, Ltd., to produce the main body and the piston in rigid opaque white plastic material.

4.1.1. Motor

Here we calculate the motor torque, which corresponds to the displacement of 10 mm that requires about 10 N force. Our twisted wire actuator uses a set of three Maxon DC motors, each of which have a nominal voltage of 18 V, a load speed of 13000 rpm, a constant torque of 12.7 mNm/A, and a maximum force of 19 N. The motors are used to apply the additional force necessary to reach the desired position, after taking into consideration the opposing tension provided by the spring. The additional force to be applied by the motor is calculated as follows:

$$f_r = 0.334 \text{ N/mm} \times 10 \text{ mm} = 3.34 \text{ N}. \quad . \; . \; (18)$$

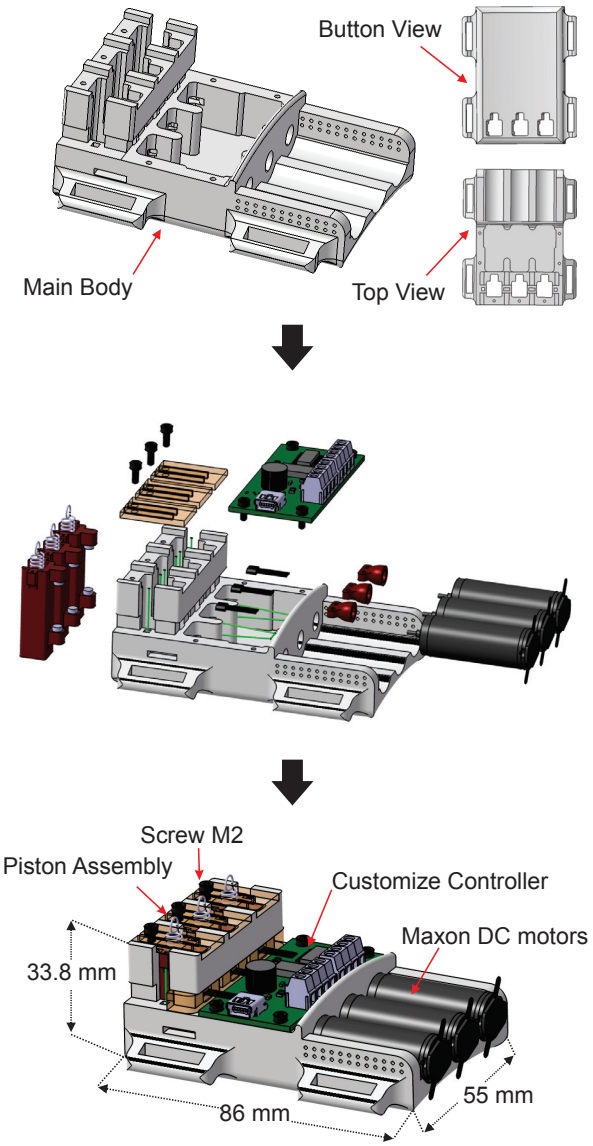

Fig. 8. Schematic view of the haptic interface, including the twisted wire actuator.

We enter the following values into Eq. (3): $A = 7$ mm, $d = 35$ mm and the wire radius equals 0.15 mm. The motor shaft rotation will then be:

$$\Delta L = 10 = \sqrt{(0.15\theta + 7)^2 + 35^2} - \sqrt{7^2 + 35^2} \quad (19)$$

where:

$$\theta = 149.16 \text{ rad}. \quad . \; . \; . \; . \; . \; . \; . \; . \; . \; . \; . \; . \; (20)$$

By adding all the given dimensions, including the spring force, the maximum applied force, and the corrected shaft ratio, we can obtain the Rc_m and τ_m of the system.

$$Rc_m = 1.7034 = 2.65 \frac{0.15\theta + 7}{\sqrt{(0.15\theta + 7)^2 + 35^2}} - 0.0002 \quad . \; (21)$$

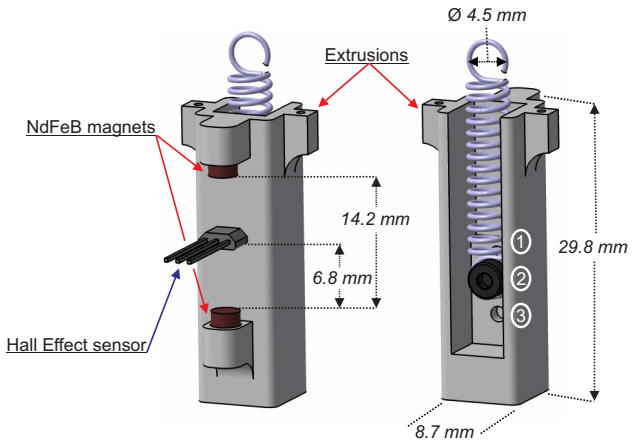

Fig. 9. Pressure piston that is integrated with the haptic device.

And the maximum torque is:

$$\tau_m = (f_m + f_r) \times Rc_m \quad . \quad . \quad . \quad . \quad . \quad . \quad . \quad . \quad . \quad . \quad (22)$$

$$\tau_m = (10 + 3.34) \times 1.7034 = 22.72 \quad . \quad . \quad . \quad . \quad . \quad (23)$$

4.1.2. Wire

We used a synthetic fiber spectra that is sold under the name Dyneema. This wire has a very small diameter of 0.15 mm, but it is still highly flexible, durable, and rigid. Dyneema is typically used in the aviation industry, but it has also appeared in the field of robotics [37, 38].

4.2. Pistons

The pistons are the most complex aspect of the design, as they require many components to be integrated within their small casings so that they can safely apply pressure to the human subject. In our design, three pistons are embedded in the main body of the device. As can be seen from **Fig. 9**, we designed the pistons to have extrusions on each side so that the wires could be threaded through the holes in the extrusions.

4.2.1. Sensor and Magnets

As there is no encoder in the system, the only way to know the position of the pistons is to use an external sensor to measure either the motor rotation or the pistons' movement. For this purpose, we used a linear Hall Effect sensor (SS495) made by Honeywell, Ltd. The 1 mm thick sensor is positioned in the middle of the 14.2 mm gap between the two small NdFeB neodymium N40 magnets (3.18 mm diameter $\times$ 9.53 mm length), as presented in [39]. The sensor provides an accurate position of the pistons by sending a non-noisy analogue signal ranging between 0 and 5 V.

4.2.2. Springs

The size of the springs plays a critical role in determining how much force will be applied to the pistons to return them to their initial position. The main consideration when selecting a spring is usually the weight of the piston. However, in our case the pistons are so small that their weight is negligible, so we sought only to use the smallest springs possible. The strength of the springs does not matter, but they must be able to stretch to 10 mm. We decided to use ultra-precision extension springs with loop ends from McMaster-Car, Ltd. These springs offer outstanding wear resistance, making them perfect for our applications. **Fig. 9** shows the three positions at which the spring may be set within the piston, as indicated by the numbers ①, ②, and ③. These three positions were implemented so that the spring's strength could be matched to the needs of the user. For instance, if the device is attached to the user's wrist, the spring should be set at position ③. There is not much fat at the human wrist area, so the looser spring will allow the piston to rebound more quickly from the hard surface. If the device is instead attached to a fleshier part of the person's forearm, the spring should be set at position ①, so the tighter coils will cause the piston to rebound more slowly, allowing the piston to sink further into the skin.

5. Evaluation of the Proposed Haptic Apparatus

In this section the haptic interface is evaluated using force and position tests. Both tests are conducted to determine the real-time positioning of the piston and the intensity of the applied forces. In task-oriented conditions, these two parameters play a critical role in the proper functioning of the mechanism.

5.1. Force Test

We hope that our haptic device will provide feedback to amputees so that they can have better control over their prosthetic limbs. This means that when a robotic hand grasps an object, the piston should apply orthogonal force feedback to the user that corresponds to the level of grasping force that is applied by the prosthetic fingers. Before we can test the accuracy of the device, we need to make sure it is capable of applying a certain range of forces to the user. To do this, we conducted a series of force tests.

The device was placed upside down and fixed on a force test stand (Mark-1 ES20), as shown in **Fig. 10**. The force test stand was equipped with a digital force gauge (Mark-10 M4-10) capable of measuring forces from 0.5 N to 2500 N, and a digital displacement gauge (Mitutoyo 543-693) with 1 μm accuracy. We carried out the experiment by running four input voltages into the device, of 5 V, 10 V, 15 V and 18 V. Although the manufacturer's description of the Maxon DC motor states that it performs best at a level of 12–15 V for long-term operations, we wanted to test the device's performance at a higher voltage level. However, since our device is of course intended for long-term use, we will focus on 15 V in our discussion of the results of the test.

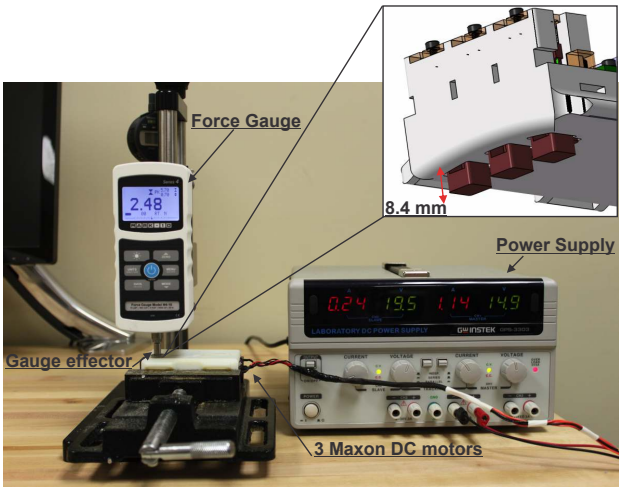

Fig. 10. Setup of the force tests.

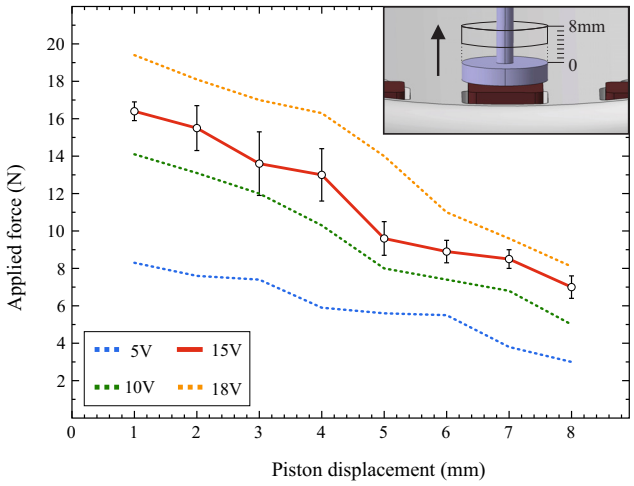

Fig. 11. Results obtained from the force tests.

To start the test, the gauge effector is tangentially placed on top of the pistons so that the display indicates zero applied force. We then manually set the gauge effector at 1 mm above the initial position (**Fig. 11** top right) by very slowly turning the handle installed at the top of the force gauge. After 1 mm of displacement, the force applied from the pistons was measured using the force gauge. This experiment was continued for seven subsequent distances, rising by increments of 1 mm, until the displacement reached 8 mm, which is approximately the maximum possible displacement.

Figure 11 shows the input voltages, the applied forces from the piston, and the variance bar for each travelled distance. As can be seen, the haptic device is capable of applying forces between 2.9 N and 16.6 N, depending on the input voltage, before reaching the maximum position. This range of force seems sufficient to inform the user of the gripping force magnitude during low-intensity tasks, such as grasping a cup of tea or squeezing a soft ball. However, in order for the piston to reach its desired position, the haptic device must be applied to an area of the

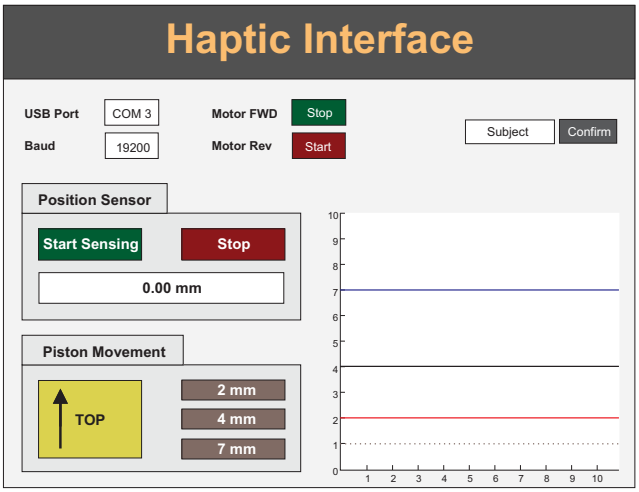

Fig. 12. Haptic interface in GUI-MATLAB for real-time control over the positioning of the piston.

body that has a certain amount of rigidity (rather than, for instance, a cellulite-ridden thigh). Note also that **Fig. 11** shows that whenever the piston moves further away from its initial position, less pressure will be applied to the user.

5.2. Position Test

After determining the maximum force, it is important to estimate the positioning accuracy of the device during real-time operation. We used a GUI MATLAB interface, shown in **Fig. 12**, and a PID controller with a sampling time of 0.1 milliseconds for this experiment.

For the test, the piston is positioned 1 mm above its initial position, and three other displacement levels, of 7 mm, 2 mm and 4 mm, were randomly given over a period of 15 seconds (taking the 2.5 s preparation time into consideration). The piston remained in the desired positions for 5 s, 5 s, and 2.5 s, respectively. The results are presented in **Fig. 13**, where the non-curved line indicates the desired value, and the curved line indicates the real-time positioning of the piston.

Based on the results we obtained, we can now define some of the critical features of the system: the time constant, the rise time, and the response time.

5.2.1. Time Constant

The time constant, λ, represents the time that it takes the piston to reach $1-1/e \approx 63.2\%$ of the desired value. We calculate the positions at which λ occurs as follows:

$$Position_x = (x - x_{-1}) \times 0.63 + x_{-1}. \quad \ldots \quad (24)$$

In the test, we placed the piston at positions of 7 mm, 2 mm, and 4 mm. When we replace the value of x with these values, and consider 1 mm to be the initial position, the formula tells us that the critical positions are 4.78 mm, 3.85 mm, and 3.26 mm. According to **Fig. 13**, the three corresponding time constants are 0.48 s, 0.49 s, and 0.08 s. Therefore, the total processing times are 2.98 s, 7.99 s, and 12.58 s.

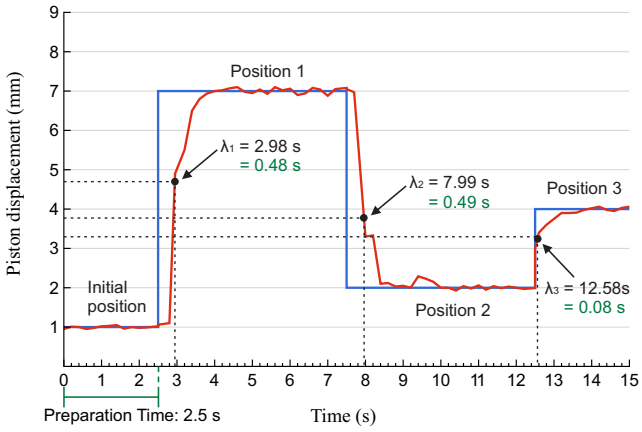

Fig. 13. Desired and real-time positioning of the piston, along with the time constants.

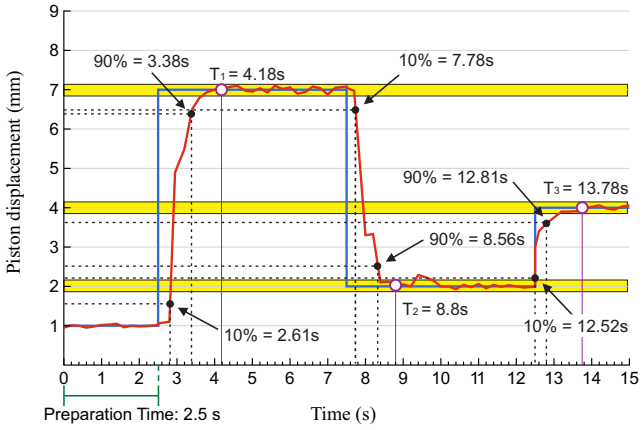

Fig. 14. Desired and real time positioning of the piston along with the rise and response times.

5.2.2. Rise Time

The rise time (T_m) is the time taken by the piston to go from 10% to 90% of the desired value. In order to calculate the three values of T_m in our system, six positions should be used:

$$Position_x = (x - x_{-1}) \times 0.1 + x_{-1} \quad . \; . \; . \; . \quad (25)$$

$$Position_{x_{+1}} = (x - x_{-1}) \times 0.9 + x_{-1} \quad . \; . \; . \; . \quad (26)$$

After replacing the constant values, the six described positions are 1.6 mm, 6.4 mm, 6.5 mm, 2.5 mm, 2.2 mm, and 3.8 mm. Taking into consideration that $T_m = T_{90\%} - T_{10\%}$, **Fig. 14** shows that the first rise time is equal to 0.77 s, the second is 0.78 s, and the third is 0.23 s, with an average of 0.59 s for the whole system.

5.2.3. Response Time

The final critical feature of the PID controller is the response time, or the time that the piston takes to react to a given input. In **Fig. 14**, the three horizontal bars represent the range of $\pm 2\%$ for each given displacement level.

In the spatial interval of 6.86 mm and 7.14 mm, the system becomes perfectly stable at 3.9 s, which is 1.4 s after the initial rise shown in **Fig. 14**. Then, in the second and third spatial intervals, the system becomes perfectly stable at 9.4 s and 13.1 s, respectively. For the second spatial interval, this is 1.9 s after the second rise time, and for the third spatial interval, this is 0.6 s after the third rise time. Overall, the response time of the haptic device requires an average of 1.3 s to attain $\pm 2\%$ of the desired stability level.

Our experiments proved that the piston is large enough to reach 8 mm, and that the required positioning features, including the time constant, the rise time, and the response time, are sufficient for the proper operation of the mechanism. Therefore, our results confirm the functionality of the haptic apparatus.

6. Discussion

This paper presented the development of a novel haptic device based on a twisted wire actuator. Our main goal was to apply vertical pressure, corresponding to the grasping force of robotic fingers, to the skin of the unimpaired human forearm. We conducted an investigation of this technique in which we calculated the model kinematic and static limitations. We thoroughly discussed the design process and the implemented equipment. Finally, we tested the apparatus through several experiments and verified its functionality.

Further research should focus on improving the device. It currently contains three pistons, but it requires five pistons to stimulate haptic feedback that will correspond to the five fingers of an advanced prosthetic hand. In addition, the effect of slippage is another piece of information that could be conveyed to the user. Haptic feedback could be carried out for this purpose using the vibrations that are caused when prosthetic fingers slide across an object's surface.

The next stage of our research will seek to integrate a vibrotactile actuator within our device. We hope to investigate the impact of superposing vibrotactile and normal stress stimuli. Our current haptic device can apply pressure that corresponds to the grasping force that is applied when the prosthetic hand grasps an object such as a cup of tea. If the amputee uses the robotic hand to grasp a cup while the hand's fingers move across its surface, perhaps normal force and vibrotactile stimuli can be superposed so that the normal force represents the grasping force, and the vibrotactile stimulation represents the vibrations resulting from the fingers' movements.

Our future work will also require us to study the difference between the touch sensitivity of robotic finger pads, and the touch sensitivity of areas of the human body. For instance, when the prosthetic hand touches an object, its sensitive fingertips will detect the amount of pressure that is being applied. However, when this pressure is then transmitted to the user's forearm via the haptic device, the person may not be able to sense the exact same amount

of pressure. Even if it is applied accurately, the human forearm may be less sensitive to pressure than the robotic finger pads, and so the haptic device will have to compensate by applying slightly more pressure to the forearm. We might investigate this by asking subjects to estimate the level of pressure that the device applies, and then comparing this estimate to the actual pressure that was applied by both the haptic device and the prosthetic fingertips in the hopes of properly calibrating the sensory feedback.

We have developed a haptic device for pressure application using an improved twisted wire actuator. However, the robotics community has not yet developed a haptic device capable of simultaneously delivering vertical pressure, shear, and temperature sensation. As we proceed towards this goal, there is much work to be done in optimizing each of these functions in turn, before they can be brought together in one unified haptic system.

Acknowledgements

This work was supported by the Natural Sciences and Engineering Research Council of Canada (NSERC) and the Ministère du Dévelopement Économique, de l'Innovation et de l'Exportation du Québec (MDEIE).

References:

[1] B. Hannaford and A. Okamura, "Haptics," B. Siciliano and O. Khatib (Eds.), Springer Handbook of Robotics, pp. 719-739, Springer Berlin Heidelberg, 2008.

[2] A. Agovic, S. Levine, N. Papanikolopoulos, and A. Tewfik, "Haptic interface design considerations for scrub nurse robots in microsurgery," 2010 18th Mediterranean Conf. on Control Automation (MED), pp. 1573-1578, June 2010.

[3] M. Evans, D. Wallace, D. Cheshire, and B. Sener, "An evaluation of haptic feedback modelling during industrial design practice," Design Studies, Vol.26, No.5, pp. 487-508, 2005.

[4] C.-H. King, M. Culjat, M. Franco, C. Lewis, E. Dutson, W. Grundfest, and J. Bisley, "Tactile Feedback Induces Reduced Grasping Force in Robot-Assisted Surgery," IEEE Trans. on Haptics, Vol.2, No.2, pp. 103-110, April 2009.

[5] H. Tanaka and K. Kushihama, "Haptic vision – vision-based haptic exploration," Proc. 16th Int. Conf. on Pattern Recognition, Vol.2, pp. 852-855, 2002.

[6] K. Kim and J. Colgate, "Haptic Feedback Enhances Grip Force Control of sEMG-Controlled Prosthetic Hands in Targeted Reinnervation Amputees," IEEE Trans. on Neural Systems and Rehabilitation Engineering, Vol.20, No.6, pp. 798-805, Nov. 2012.

[7] P. Srinivasa, S. Nagananda, G. Kadambi, R. Hariharan, P. Shankpal, and S. Shankapal, "Development of two degree of freedom (DoF) bionic hand for below elbow amputee," 2013 IEEE Int. Conf. on Electronics, Computing and Communication Technologies (CONECCT), pp. 1-6, Jan. 2013.

[8] S. Takamuku, A. Fukuda, and K. Hosoda, "Repetitive grasping with anthropomorphic skin-covered hand enables robust haptic recognition," IEEE/RSJ Int. Conf. on Intelligent Robots and Systems (IROS 2008), pp. 3212-3217, Sep. 2008.

[9] P. Galambos and P. Baranyi, "Vibrotactile force feedback for telemanipulation: Concept and applications," 2011 2nd Int. Conf. on Cognitive Infocommunications (CogInfoCom), pp. 1-6, July 2011.

[10] J. Martinez, D. Martinez, J. Molina, P. Gonzalez, and A. Garcia, "Comparison of Force and Vibrotactile Feedback with Direct Stimulation for Texture Recognition," 2011 Int. Conf. on Cyberworlds (CW), pp. 62-68, Oct. 2011.

[11] T. Sono, L. Menegaldo, and M. Pinotti, "Hand prosthesis prototype controlled by EMG and vibrotactile force feedback," 5th IEEE RAS EMBS Int. Conf. on Biomedical Robotics and Biomechatronics, pp. 91-95, Aug. 2014.

[12] C. Hager-Ross, K. Cole, and R. Johansson, "Grip-force responses to unanticipated object loading: load direction reveals body- and gravity-referenced intrinsic task variables," Experimental Brain Research, Vol.110, No.1, pp. 142-150, 1996.

[13] S. J. Lederman and R. L. Klatzky, "Haptic perception: A tutorial," Attention, Perception, & Psychophysics, Vol.71, No.7, pp. 1439-1459, 2009.

[14] J. C. Lee, P. H. Dietz, D. Leigh, W. S. Yerazunis, and S. E. Hudson, "Haptic Pen: A Tactile Feedback Stylus for Touch Screens," Proc. of the 17th Annual ACM Symposium on User Interface Software and Technology, UIST '04, pp. 291-294, New York, NY, USA, 2004.

[15] D. Caldwell, N. Tsagarakis, and C. Giesler, "An integrated tactile/shear feedback array for stimulation of finger mechanoreceptor," Proc. 1999 IEEE Int. Conf. on Robotics and Automation, Vol.1, pp. 287-292, 1999.

[16] A. M. Okamura, J. T. Dennerlein, and R. D. Howe, "Vibration feedback models for virtual environments," Proc. 1998 IEEE Int. Conf. on Robotics and Automation, Vol.1, pp. 674-679, 1998.

[17] D. Damian, M. Ludersdorfer, Y. Kim, A. Hernandez Arieta, R. Pfeifer, and A. Okamura, "Wearable haptic device for cutaneous force and slip speed display," 2012 IEEE Int. Conf. on Robotics and Automation (ICRA), pp. 1038-1043, 2012.

[18] J. Dargahi and S. Najarian, "Human tactile perception as a standard for artificial tactile sensing – a review," The Int. J. of Medical Robotics and Computer Assisted Surgery, Vol.1, No.1, pp. 23-35, 2004.

[19] E. P. Gels, "Electroactive polymer (EAP) actuators as artificial muscles: reality, potential, and challenges," Y. Bar-Cohen (Eds.), SPIE, 2004.

[20] E. Smela, "Conjugated polymer actuators for biomedical applications," Advanced Materials, Vol.15, No.6, pp. 481-494, 2003.

[21] F. Bechet and K. Ohnishi, "An experimental validation of electro-hydraulic transmission for haptic teleoperation – Comparison with thrust wire –," 2014 IEEE 23rd Int. Symposium on Industrial Electronics (ISIE), pp. 1174-1179, June 2014.

[22] R. Fan, M. Culjat, C.-H. King, M. Franco, R. Boryk, J. Bisley, E. Dutson, and W. Grundfest, "A Haptic Feedback System for Lower-Limb Prostheses," IEEE Trans. on Neural Systems and Rehabilitation Engineering, Vol.16, No.3, pp. 270-277, 2008.

[23] P. Berkelman, R. Hollis, and S. Salcudean, "Interacting with virtual environments using a magnetic levitation haptic interface," Proc. 1995 IEEE/RSJ Int. Conf. on Intelligent Robots and Systems, 'Human Robot Interaction and Cooperative Robots,' Vol.1, pp. 117-122 1995.

[24] O. Erol and H. Gurocak, "Mr-brake with permanent magnet as passive actuator for haptics," World Haptics Conf (WHC) 2013, pp. 413-418, April 2013.

[25] V. Duchaine and A. Rana, "Dielectric geometry for capacitive-based tactile sensor," WO Patent App. PCT/CA2014/050,040, July 24, 2014.

[26] S. R. Kremer, "Twisted cord actuator," US Patent 4,843,921, July 4, 1989.

[27] M. Shoham, "Twisting wire actuator," J. of Mechanical Design, Vol.127, No.3, pp. 441-445, 2005.

[28] T. Wurtz, C. May, B. Holz, C. Natale, G. Palli, and C. Melchiorri, "The twisted string actuation system: Modeling and control," 2010 IEEE/ASME Int. Conf. on Advanced Intelligent Mechatronics (AIM), pp. 1215-1220, 2010.

[29] S. Kawamura, W. Choe, S. Tanaka, and S. R. Pandian, "Development of an ultrahigh speed robot FALCON using wire drive system," Proc. 1995 IEEE Int. Conf. on Robotics and Automation, Vol.1, pp. 215-220, 1995.

[30] I. Godler, K. Hashiguchi, and T. Sonoda, "Robotic finger with coupled joints: a prototype and its inverse kinematics," 2010 11th IEEE Int. Workshop on Advanced Motion Control, pp. 337-342, 2010.

[31] T. Sonoda and I. Godler, "Multi-fingered robotic hand employing strings transmission named "Twist Drive"," 2010 IEEE/RSJ Int. Conf. on Intelligent Robots and Systems (IROS), pp. 2733-2738, 2010.

[32] M. C. Jimenez and J. A. Fishel, "Evaluation of force, vibration and thermal tactile feedback in prosthetic limbs," 2014 IEEE Haptics Symposium (HAPTICS), pp. 437-441, 2014.

[33] K. Kim, J. Colgate, J. Santos-Munne, A. Makhlin, and M. Peshkin, "On the Design of Miniature Haptic Devices for Upper Extremity Prosthetics," IEEE/ASME Trans. on Mechatronics, Vol.15, No.1, pp. 27-39, Feb. 2010.

[34] M. Konyo, "Wearable haptic interface using icpf actuators for tactile feel display in response to hand movements," J. of Robotics and Mechatronics, Vol.15, No.2, pp. 219-226, 2003.

[35] H. Tanaka, H. Kaminaga, and Y. Nakamura, "Pressure Feedback Control Based on Singular Perturbation Method of an Electro-Hydrostatic Actuator for an Exoskeletal Power-Assist System," J. of Robotics and Mechatronics, Vol.24, No.2, pp. 354-362, 2012.

[36] M. Suzuki and A. Ichikawa, "Toward springy robot walk using Strand-muscle actuators," Proc. 7th Int. Conf. on Climbing and Walking Robots, pp. 479-486, 2005.

[37] J.-D. Deschenes, P. Lambert, S. Perreault, N. Martel-Brisson, N. Zoso, A. Zaccarin, P. Hébert, S. Bouchard, and C. M. Gosselin, "A cable-driven parallel mechanism for capturing object appearance from multiple viewpoints," Proc. of the Sixth Int. Conf. on 3-D Digital Imaging and Modeling (3DIM 2007), pp. 367-374, 2007.
[38] M. J.-d. Otis, T.-L. Nguyen-Dang, T. Laliberté, D. Ouellet, D. Laurendeau, and C. Gosselin, "Cable tension control and analysis of reel transparency for 6-dof haptic foot platform on a cable-driven locomotion interface," Int. Conf. on Intelligent Control Systems Engineering, Vol.3, No.1, pp. 16-29, 2009.
[39] S. Kim, M. Spenko, S. Trujillo, B. Heyneman, V. Mattoli, and M. R. Cutkosky, "Whole body adhesion: hierarchical, directional and distributed control of adhesive forces for a climbing robot," 2007 IEEE Int. Conf. on Robotics and Automation, pp. 1268-1273, 2007.

Name:
M. Reza Motamedi

Affiliation:
Ph.D. Candidate, Department of Automated Manufacturing Engineering, École de Technologie Supérieure (ÉTS)

Address:
1100 Rue Notre-Dame Ouest, Montreal H3C 1K3, Canada

Brief Biographical History:
2011 Received M.Sc. in Mechatronics Systems, Kingston University, London, United Kingdom
2015- Ph.D. Candidate in Haptics (Mechatronics and Robotics), École de Technologie Supérieure

Main Works:
• haptics, rehabilitation robotics

Membership in Academic Societies:
• The Institute of Electrical and Electronics Engineers (IEEE)

Name:
David Florant

Affiliation:
Department of Automated Manufacturing Engineering, École de Technologie Supérieure (ÉTS)

Address:
1100 Rue Notre-Dame Ouest, Montreal H3C 1K3, Canada

Name:
Vincent Duchaine

Affiliation:
Professor, Department of Automated Manufacturing Engineering, École de Technologie Supérieure (ÉTS)

Address:
1100 Rue Notre-Dame Ouest, Montreal H3C 1K3, Canada

Brief Biographical History:
2010 Received Ph.D. in Mechanical Engineering, Université Laval
2010- Post-doctoral Fellow, Stanford University
2010- École de Technologie Supérieure

Main Works:
• control and sensing for physical human-robot interaction

Membership in Academic Societies:
• The Institute of Electrical and Electronics Engineers (IEEE)